JGR Oceans

RESEARCH ARTICLE
10.1029/2019JC015338

Key Points:
- The vertical shear between the BC and the IWBC dissipates turbulent kinetic energy
- The vertical shear overcomes the stratification at the BC-IWBC boundary leading to an enhancement of the vertical diffusivity
- The shear and nutrient gradient between the BC and the IWBC generate a vertical turbulent nitrate flux

Correspondence to:
C. Z. Lazaneo,
cauezlazaneo@usp.br

Citation:
Lazaneo, C. Z., Napolitano, D. C., da Silveira, I. C. A., Tandon, A., MacDonald, D. G., Ávila, R. A., Calil, P. H. R. (2020). On the role of turbulent mixing produced by vertical shear between the Brazil Current and the Intermediate Western Boundary Current. *Journal of Geophysical Research: Oceans*, *125*, e2019JC015338. https://doi.org/10.1029/2019JC015338

Received 31 MAY 2019
Accepted 25 DEC 2019
Accepted article online 14 JAN 2020

On the Role of Turbulent Mixing Produced by Vertical Shear Between the Brazil Current and the Intermediate Western Boundary Current

Cauê Z. Lazaneo[1], Dante C. Napolitano[1], Ilson C. A. da Silveira[1], Amit Tandon[2], Daniel G. MacDonald[2], Rafael A. Ávila[3], and Paulo H. R. Calil[4]

[1]Instituto Oceanográfico, Universidade de São Paulo, São Paulo, Brazil, [2]College of Engineering, University of Massachusetts Dartmouth, Dartmouth, MA, USA, [3]Instituto de Oceanografia, Universidade Federal do Rio Grande, Rio Grande, Brazil, [4]Institute of Costal Research, Helmholtz-Zentrum Geesthacht, Geesthacht, Germany

Abstract An intensification of the vertical shear is observed below the surface mixed layer at 21°S due to the mutually opposing flows of the Brazil Current and the Intermediate Western Boundary Current. The propensity to develop turbulence and mixing due to vertical shear over intense stabilizing density gradients is an important characteristic of such environments. For the first time, microscale measurements were made in the Brazil Current-Intermediate Western Boundary Current system, providing direct quantitative values of the turbulent fluctuations. Peaks of relative strong dissipation rates of turbulent kinetic energy ($O(10^{-8})$ W/kg) were observed close to the base of the surface mixed layer. On the other hand, prominent peaks of turbulent kinetic energy dissipation rates of up to 2 orders of magnitude higher than the background were observed at deeper levels, where stratification begins to lose intensity. Analyzing such peaks, caused by intense vertical shear or weak stratification—and sometimes both—, allows a characterization of the local mixing processes and the role played by vertical exchanges of biogeochemical properties. Based on the estimated nitrate gradient and the vertical diffusivity, we show that turbulent mixing driven by vertical shear plays an important role in the supply of nitrate to the upper layer.

Plain Language Summary Turbulent mixing across the density surfaces can bring nutrient-rich waters from the subsurface to the upper sunlit layer of the ocean, therefore, modulating the primary productivity in an oligotrophic ocean. Based on measurements of small-scale shear variance, we found that the interaction between the poleward-flowing Brazil Current and the Intermediate Western Boundary Current flowing underneath in the opposite direction enhances the upper-ocean mixing through shear instabilities. The destabilizing influence of the velocity shear overcomes the stabilizing effect of the stratification. The mixing on the interface between these two western boundary currents may provide an important route for local nutrient exchanges.

1. Introduction

The Brazil Current (BC) is the western boundary current that closes the South Atlantic Subtropical Gyre. It is unique among poleward-flowing western boundary currents in that its vertical structure changes along its extent (Boebel et al., 1999; Stramma & England, 1999). The BC originates from the bifurcation of the surface branch of the South Equatorial Current around 15°S (Soutelino et al., 2011). Between its origin and approximately 20°S, the BC is an eddy-dominated, mixed-layer jet transporting Tropical Water in the upper 200 m of the water column (Soutelino et al., 2011). 21°S marks the latitude of the South Atlantic Central Water flow bifurcation at the pycnocline, where this nutrient-rich and less salty water mass feeds the BC in its poleward flow. Below the pycnocline, the equatorward flow of the Intermediate Western Boundary Current (IWBC) is formed due to the bifurcation of the colder, fresher, and nitrate-richer Antarctic Intermediate Water flow (Boebel et al., 1999). Between 26°S and 21°S, the IWBC interacts with the poleward flow of the BC, enhancing the vertical shear and property gradients. According to Silveira et al. (2004), the BC-IWBC system is a baroclinic current system with a single distinct flow reversal between the upper and intermediate portions of the continental slope. The reverse flow of the BC-IWBC in the upper 400 m enhances the vertical shear in the interior ocean and may dissipate energy through small-scale processes such as vertical mixing. Mixing in this region is one of the least understood physical processes that may control stratification, primary production, carbon exchanges, and heat and dissolved material (nutrients) exchanges through diapycnal transport (Gregg, 1987). A better knowledge of turbulent processes, including the dissipation of turbulent kinetic energy (TKE), is fundamental to our understanding of ocean mixing and the distribution of heat, salt, and biogeochemical components in the ocean (Gargett, 1997).

Ocean circulation is characterized by a wide range of scales of motion, and its main energy sources are well known (Ferrari & Wunsch, 2009). The work of wind stress on the surface of the ocean is the primary source of energy input to the ocean. Although relatively small compared to wind stress, the effects of heating (cooling) and precipitation (evaporation) are also relevant. On the other hand, the sink of energy and its mechanisms are far less well understood (e.g., D'Asaro et al., 2011). To achieve energy dissipation, a forward cascade of energy is required from motions ranging from ocean-basin scales to the viscous, centimeter scales (e.g., D'Asaro et al., 2011). Instabilities of the large-scale circulation lead to the generation of mesoscale eddies, which are commonly recognized from satellite altimetry and quasi-synoptic hydrographic data, and may be simulated by numerical models with relatively coarse spatial resolution; on submesoscale, stirring and straining by eddies and filaments of order 1–10 km in the mixed layer may invoke secondary instabilities (e.g., Nagai et al., 2008); from this stage on, these secondary instabilities can evolve down the forward energy cascade, leading ocean-basin scale to the viscous, centimeter-scale motions and ultimately energy dissipation (McWilliams, 2016). However, observations of smaller-scale processes, mainly on dissipation scales (i.e., the small-scale end of the turbulent cascade; Kolmogorov, 1968) are scarce and, until now, nonexistent in the BC-IWBC domain.

Different mechanisms can extract energy from geostrophic flows through baroclinic instabilities and transfer it to unbalanced motions, from where it may be cascaded to the smallest scale (Ferrari & Wunsch, 2009; Nikurashin & Ferrari, 2011; Nikurashin et al., 2013). According to Zhai et al. (2010), western boundary regions are recognized as a sink site for the westward propagating ocean eddies, dissipating a great amount of energy in midlatitudes. The interaction of a flow over rough topography can promote strong dissipation of turbulent energy, enhancing the mixing in the interior ocean (Kunze et al., 2006; Ledwell et al., 2000; Munk & Wunsch, 1998; Polzin et al., 1997). Recent literature suggests that fronts and mixed-layer instabilities, characterized by intense density gradients and vertical shear of the horizontal velocity component (Boccaletti et al., 2007; Mahadevan et al., 2010; Ramachandran et al., 2018; Thomas et al., 2008, 2013), are also possible routes of energy dissipation (Molemaker et al., 2010).

Stratified-shear conditions occur in many ocean environments such as thermal/salinity fronts (e.g., Ramachandran et al., 2018), wind-driven flows (e.g., Gregg, 1989), and in opposing flows such as the BC-IWBC, as in the present study. The propensity to develop turbulence and mixing due to vertical shear over intense density gradients is an important characteristic of these environments. Turbulence and mixing can be generated when the destabilizing influence of shear overcomes the stabilizing influence of stratification, which is revealed by the Richardson number ($Ri = N^2/S^2$, where $N^2 = -g\rho_0^{-1}\partial\rho/\partial z$ is the stratification and $S^2 = (\partial u/\partial z)^2 + (\partial v/\partial z)^2$ is the shear intensity). The shear instabilities develop leading to turbulence if the ratio between these quantities is equal or less than a quarter (Miles, 1961). The local value of Ri in the ocean (measured in orders of magnitude) may be a useful guide to the factors leading to turbulence and can provide a means to quantify mixing (Thorpe, 2007). The generation of turbulence is frequently associated with Kelvin-Helmholtz instabilities (Thorpe, 1973). These instabilities are defined by a billow of stratified fluid that may decay into turbulence and become well mixed (Gregg, 1987). According to Gregg (1987), a perturbation in a stratified-shear condition such as the passage of a storm (e.g., Rumyantseva et al., 2015) can evolve into a roll-up of stratified fluid until it overcomes the buoyancy force and the feature collapses into disorganized motions. The last stage of this is turbulence, and earlier stages are considered preturbulent stages (e.g., MacDonald et al., 2013).

Turbulence observations near the Kuroshio Current suggest that, on the cyclonic side of the jet at the pycnocline (Nagai et al., 2009) and also at the surface of the ocean (D'Asaro et al., 2011), strong dissipation of TKE is associated with frontogenesis (e.g., Hoskins & Bretherton, 1972) and symmetric instability (e.g., Hoskins, 1974). Kaneko et al. (2012) investigated the turbulence structure across the Kuroshio focusing on the difference between dissipation values near to and far from the front. The mean of the turbulent energy dissipation rate was higher near fronts on both cyclonic and anticyclonic sides. However, on the cyclonic side, a strong vertical shear with higher dissipation rates was observed, where large density gradients were consistent with turbulence enhancement due to frontogenesis. Beyond the physical importance of the turbulent field, it has an essential role over the biogeochemical properties exchanges. The nitrate turbulent flux promotes the high concentration of chlorophyll-a across the Kuroshio (Kaneko et al., 2013) and can support up to 50% of the primary production in the Great Australia Bight (Doubell et al., 2018). Interior regions of high-energy dissipation due to the interaction with topography and in the upper ocean are of great interest for their potential contribution to the energy budget of the general circulation, in the maintenance of the stratification, and in the exchange of (in)organic compounds that may explain the increase in primary productivity. Turbulence occurring in the upper sunlit layer of the ocean is increasingly recognized as critical to the functioning of the marine food web (Gargett, 1997).

Here, we investigate turbulent mixing processes in the stratified-shear flow of the BC-IWBC at 21.6°S. Our specific questions are as follows: (i) Can the mutually opposing flows of these western boundary currents modulate vertical turbulent mixing? and (ii) what magnitude of property exchanges is driven by small-scale processes? To address these questions, we perform a mixing experiment at the BC-IWBC system, sampling for the first time the microstructure of this shear-stratified environment, down to approximately 400 m, and capturing the BC-IWBC interaction (section 2). In section 3, we outline a potential vorticity analysis to better understand the local dynamics at mesoscale of this shear-stratified flow. The results of the TKE dissipation rates as well as vertical diffusivities and nitrate flux are given in section 4. The discussion and the concluding remarks are posed in section 5.

2. The BC-IWBC Mixing Experiment

The BC-IWBC experiment was designed to study the interaction of the BC with the reverse flow of the IWBC underneath it. South of 21°S, where the BC acquires a typical western boundary current structure, an oceanographic survey was conducted during the austral winter (August) of 2017 aboard the *R/V Alpha-Crucis* to obtain a vertical section across the BC. This study discusses the results of a zonal vertical section at 21.6°S (Figure 1a) from the surface to 400-m depth, where it is possible to observe the poleward flow of the BC within the mixed layer and the equatorward flow of the IWBC below the pycnocline (Figures 1b and 1c).

Velocity was continuously measured in a cross section of the BC-IWBC system with a RDI-75 kHz Vessel-Mounted Acoustic Doppler Current Profiler (ADCP) in 8-m bins, and data were primarily processed by the Common Ocean Data Access System (CODAS) software, following the guidelines of Firing (1995). Hydrographic data were obtained with a Seabird CTD-Rosette with 24 Niskin bottles. Water samples for nutrient analysis were collected every 25 m down to 400-m depth, with the determination of nitrate concentrations performed using an autoanalyzer, following the modified Grasshoff method (Grasshoff et al., 2009). The quasi-synopticity of the samples was guaranteed by the positions of the eight oceanographic stations, determined by the local baroclinic radius of deformation.

Turbulent parameters were estimated from measurements of the shear variance at four stations (Figure 1a) crossing the BC-IWBC using a vertical microstructure profiler from *Rockland Scientific* (VMP-250) operating at 512 Hz. The VMP was equipped with two shear probes, one SBE7 microconductivity probe and one FP07 thermistor. During the free-falling profile, shear variance, conductivity, and temperature were measured. The VMP operated in downcast mode, with speeds varying between 1.4 m/s near the surface and 0.2 m/s near the maximum profiled depth. For statistical reliability, two VMP casts were performed at each station. Details about turbulence measurements and its calculation are given in section 4.

3. The Mesoscale Field

The estimation of the turbulent parameters (dissipation of TKE, vertical diffusivities, and vertical turbulent fluxes) was the main focus of the experiment. Nevertheless, a description of the mesoscale field is an important framework for interpreting these measurements of turbulence. An objective analysis was conducted to estimate the background mesoscale field of the meridional component (v) of the velocity (Figure 1b) and potential density (σ_θ; Figure 1c). The same correlation lengths ($\Delta x = 30$ km, $\Delta z = 100$ m) were used in both fields to reduce the error associated with different scales of the quantities in dynamic calculations, such as potential vorticity.

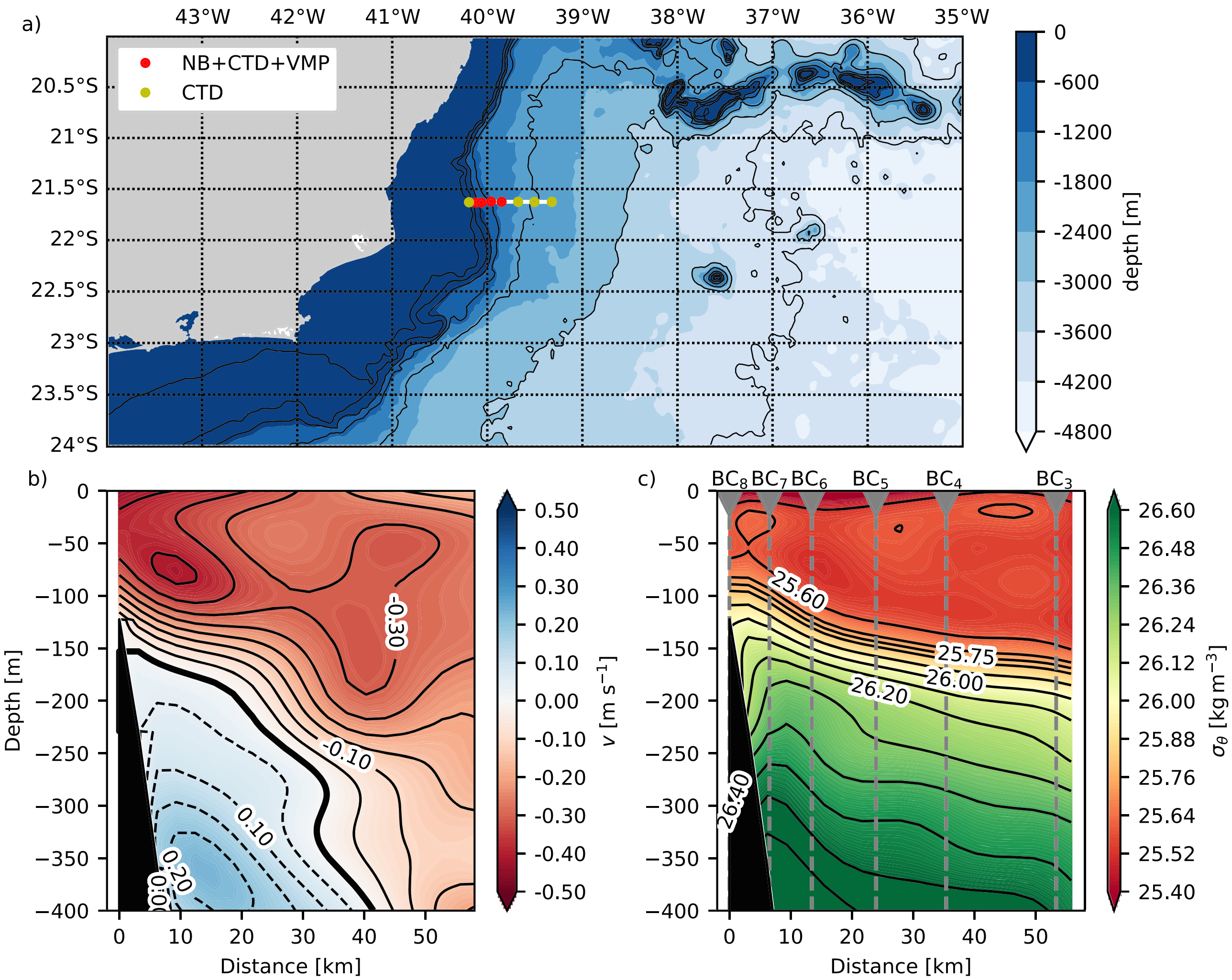

Figure 1. (a) Station map with bathymetry from ETOPO (Smith & Sandwell, 1997) in the background (colors). Black solid lines are the isobaths. Red dots represent the stations where the VMP, CTD, and Niskin bottles were deployed. Yellow dots represent the station where only the CTD was deployed. The white line represents the track of the ship continuously measuring velocity with the ADCP. (b) Vertical section of the meridional velocity estimated by the objective analysis (colors). Solid black lines represent negative isotachs, while dashed black lines represent the positive isotachs. Isotach of zero velocity is depicted as the thick solid black line. (c) Vertical section of potential density (σ_θ) estimated by the objective analysis (colors). Black contours represent the isopycnals, and vertical gray and dashed lines represent the locations of the stations with their names at the top.

The selected experimental site presents a unique vertical structure among western boundary currents. Just south of 21°S, the BC begins to acquire characteristics of a western boundary current. However, the BC sampled at 21.6°S is still a surface mixed-layer (SML) jet, confined within the upper 100–150 m of the water column (Figure 1b). The SML depth is defined as the depth at which potential density is 0.125 kg/m^3 greater than the potential density value at the surface (de Boyer Montégut et al., 2004). The isotachs of the lower BC (Figure 1b) follow the high stratification layer,

$$N^2 = \frac{\partial b}{\partial z}, \tag{1}$$

where the buoyancy is

$$b = -\frac{g}{\rho_0}\sigma_\theta. \tag{2}$$

In Figure 1c, the sloped, western boundary currents isopycnals flatten toward the offshore direction. At intermediate levels, the equatorward flow of the IWBC opposes the poleward flow of the BC. This reverse

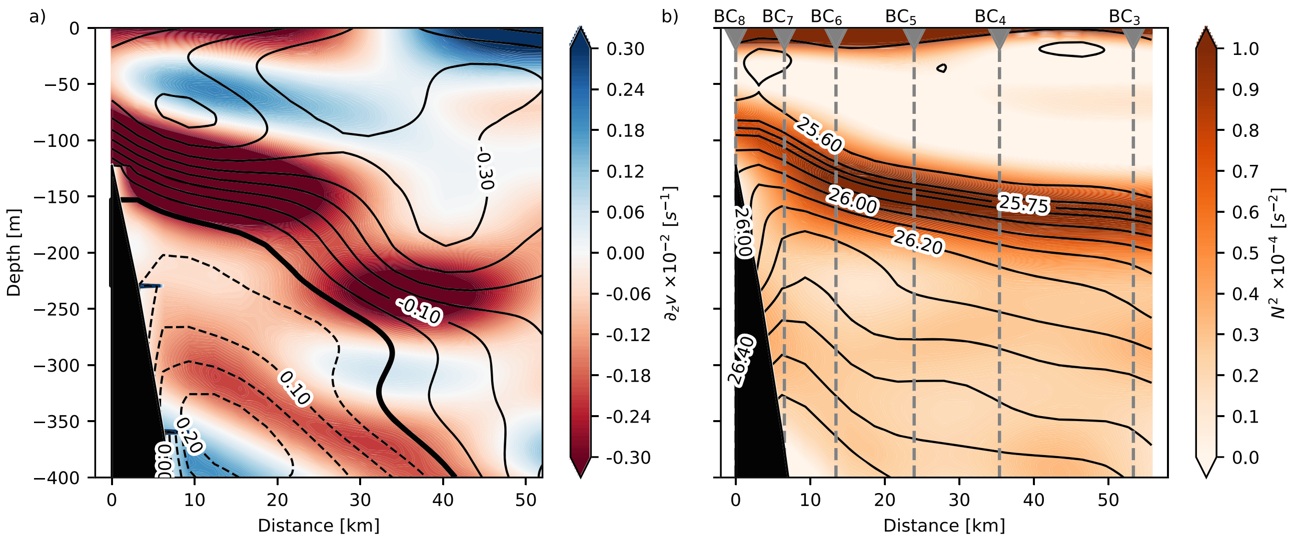

Figure 2. (a) Vertical section of the vertical shear of the meridional velocity (colors) with contours of negative (solid black lines) and positive (dashed black lines) isotachs. (b) Vertical section of the stratification (colors) with isopycnals contours. Vertical dashed gray lines show the location of the oceanographic stations.

flow creates an intense vertical shear (Figure 2a) within the higher stratification layer (Figure 2b) setting up a stratified shear flow environment.

A potential vorticity (hereafter PV) analysis is an indicative tool of the capability of the system to develop instabilities (D'Asaro et al., 2011; Thomas et al., 2008, 2013). Here, a two-dimensional PV section (e.g., Ramachandran et al., 2018; Thomas et al., 2016) is evaluated from the objective field, assuming that along-stream variations of quantities are negligible. However, these gradients could be significant, refuting the approximation of two-dimensional PV (see details in Thomas et al., 2016; Ramachandran et al., 2018). The Ertel PV is given by

$$q = (f\hat{k} + \nabla \times \mathbf{u}) \cdot \nabla b, \tag{3}$$

where f is the planetary vorticity, $\hat{k}$ is the unit vector, and $\mathbf{u} = (u, v, w)$ is the 3-D velocity vector. Given the assumptions described above, the 2-D version of (3) is

$$q \approx \left(f + \frac{\partial v}{\partial x}\right) N^2 - \frac{\partial v}{\partial z}\frac{\partial b}{\partial x}. \tag{4}$$

According to Thomas et al. (2016), (4) is expressed by a sum of two constituents that emphasizes the contrasting roles of vertical vorticity/stratification and baroclinicity. The scaled PV,

$$q \approx \frac{\left[\left(f + \frac{\partial v}{\partial x}\right) N^2 - \frac{\partial v}{\partial z}\frac{\partial b}{\partial x}\right] f}{\overline{f^2 N^2}}, \tag{5}$$

where the overbar denotes spatial averaging, is outlined in Figure 3.

No negative PV values are observed below the SML and below the pycnocline, where the IWBC flows (Figure 3a); $q < 0$ within the SML could suggest a specific type of SML instability (e.g., Thomas et al., 2013). However, the spatial resolution of the data set and the smoothing due to the objective field do not allow the diagnosis of these processes. On the other hand, one considerable patch of relative low PV is observed within the upper stratified layer (x ≈5–15 km, z ≈80–160 m in Figure 3a), as well as low PV values occur below the pycnocline. Vertical stratification and total vorticity dominate the cross-section structure below the SML. PV values close to 0 are observed below the pycnocline (Figure 3b), meaning that low relative vorticity and reduced stratification may increase the potential for the development of baroclinicity-driven instabilities. The second term, which accounts for the horizontal buoyancy gradient and the vertical shear, shows an intense patch of negative values (Figure 3c). This patch of relatively high baroclinicity is confined to the stratified layer. If the magnitude of the baroclinicity term is higher than the magnitude of the vertical vorticity/stratification, the water column should develop some instabilities.

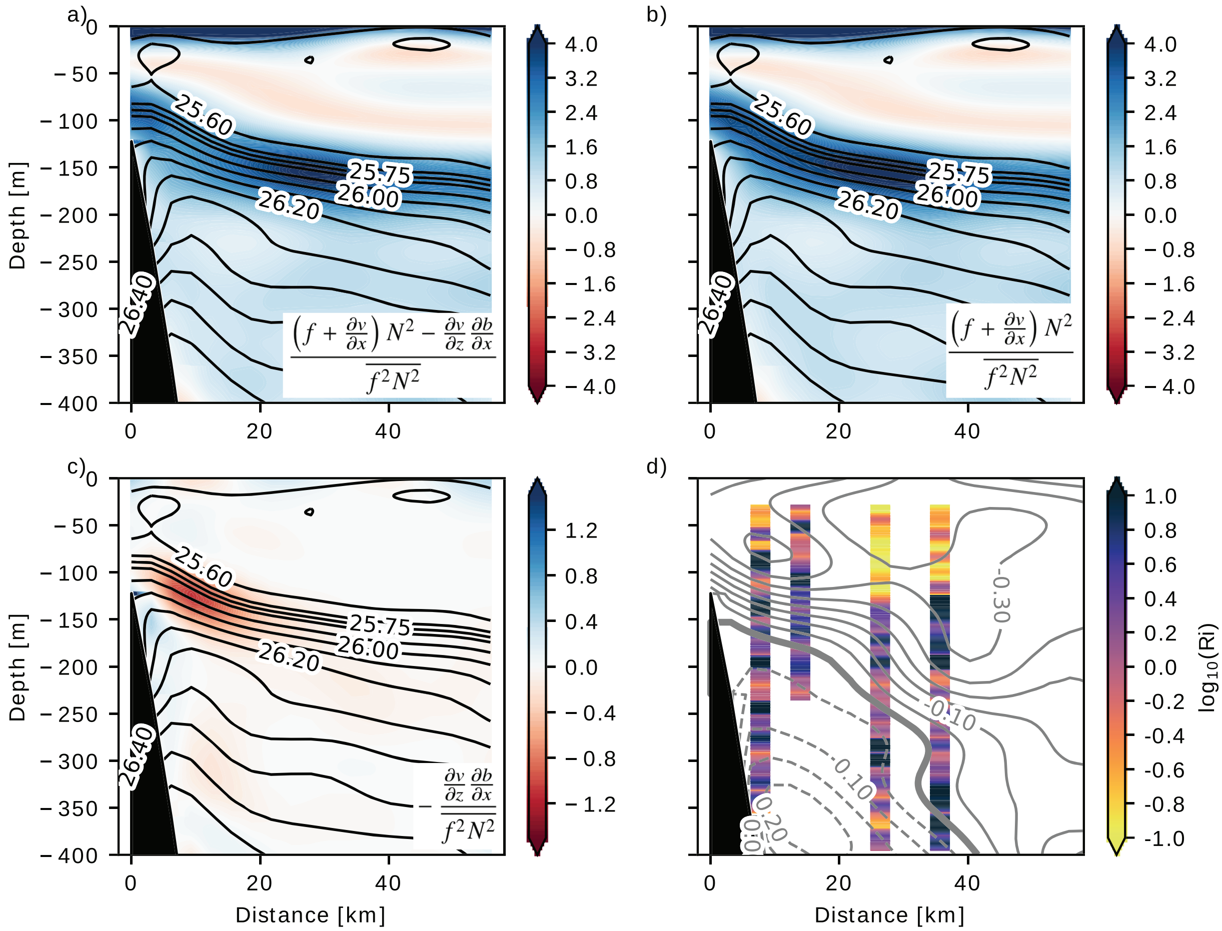

Figure 3. Vertical sections of (a) the scaled potential vorticity (total), (b) the scaled vertical vorticity/stratification term, and (c) the scaled baroclinicity term. Black contours represent isopycnals. Panel (d) is the 8-m Richardson number (*Ri*) with contours of negative (solid lines) and positive (dashed lines) isotachs.

The reduction of the PV values, as a consequence of the interaction between two strong flows, makes the flow to be in a dynamical regime marginally stable prone to instabilities. The 8-m Richardson number profiles (*Ri* hereafter) are sometimes close to Miles instability criterion and, also close to 1 even over the stabilizing effect of the stratified layer (Figure 3d). It can be an indicator of the formation of small-scale turbulence driven by the vertical shear of the local reversed flow (e.g., Balsley et al., 2008; Taylor & Ferrari, 2009). Previous studies conducted by Silveira et al. (2008) and Rocha et al. (2014) suggest that the BC-IWBC is baroclinically unstable since the horizontal vorticity gradient changes sign in the region. This criterion for baroclinic instability is also evident (not shown) in the present study. However, the competition between shear and stratification as depicted by the *Ri* profiles suggests a potential to develop shear instabilities and eventually enhanced small-scale dissipation and mixing. To elucidate the role of the vertical shear in the generation of turbulence in the region, microstructure vertical shear fluctuations along the zonal section are analyzed in section 4.

4. Turbulence Observations

4.1. Dissipation Analysis

In this study, dissipation rates of TKE are estimated using microstructure measurements. This technique for evaluating turbulence in oceanic flows has been employed in many previous studies (e.g., Itoh et al., 2010; Kaneko et al., 2012; Lueck et al., 1983; Moum & Osborn, 1986; Oakey, 1982). Microstructure analysis relies on high-frequency measurements to directly quantify turbulent fluctuations. TKE dissipation rates (ε) are estimated from the MATLAB toolbox provided by Rockland Scientific, which is based on the theory and techniques proposed in the literature (Gargett, 1997; Gregg, 1999; Oakey, 1982; Wolk et al., 2002). The microscale shear variance is used to obtain ε from the integration of the spectrum of velocity fluctuations

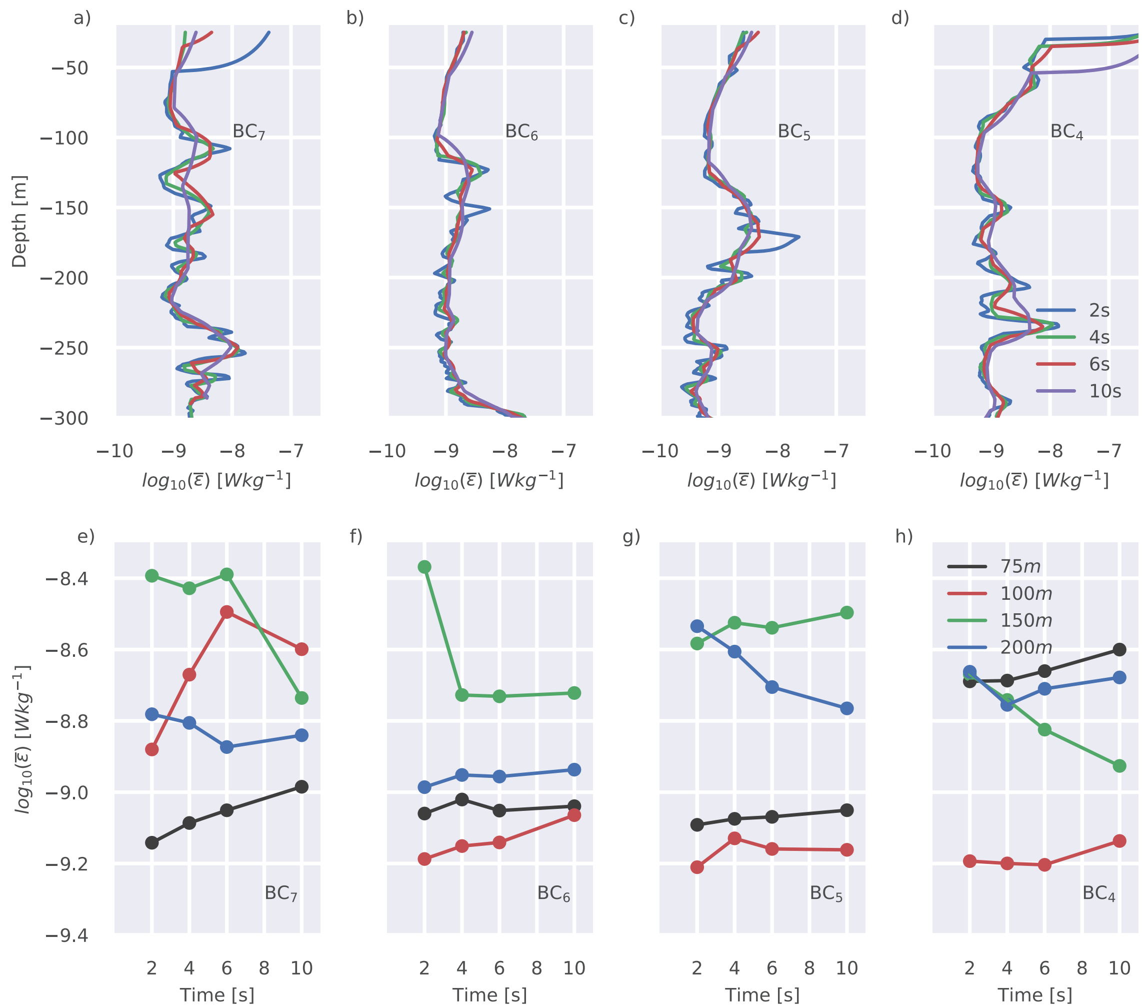

Figure 4. Panels are organized from left to right as a function of stations. Panels (a) and (e) represent station BC_7, (b) and (f) represent station BC_6, (c) and (g) represent station BC_5, and panels (d) and (h) represent the station BC_4. Panels (a), (b), (c), and (d) represent the vertical profile of dissipation rates on logarithmic scales using 2 s (blue), 4 s (green), 6 s (red), and 10 s (purple). Panels (e), (f), (g), and (h) represent the variation of dissipation rates among those segments at 75 m (black), 100 m (red), 150 m (green), and 200 m (blue).

(Φ) for segments of the water column,

$$\varepsilon = \frac{15}{2}\nu\overline{\left(\frac{\partial u'}{\partial z}\right)^2} = \frac{15}{2}\nu\int_1^{k_{max}}\Phi(k)\mathrm{d}k \quad [\mathrm{W/kg}], \tag{6}$$

where ν is the kinematic molecular viscosity and k_{max} is the maximum wavenumber determined by the fast Fourier transform with 50% overlap for each vertical segment. The shear variance is computed by integrating the shear power spectrum from the lowest wavenumber k_1, set to 1 cycle per meter, to the highest wavenumber k_{max}, where the shear spectrum presents a minimum between the natural spectrum and a high wavenumber peak close to noise level. If the wavenumber of minimum energy is smaller than that corresponding to the Kolmogorov turbulent scale [$\eta = (\nu^3\varepsilon^{-1})^{0.25}$], the integration is extended to k_{max} along the Nasmyth spectral form (e.g., Oakey, 1982). In other words, ε is proportional to the area under the shear spectrum for homogeneous and isotropic turbulence. The spectral shapes of $\Phi(k)$ in the range below k_{max} agreed well with those of the Nasmyth spectrum (not shown), indicating small systematic error (Wolk et al., 2002). The dissipation rates were assumed reliable by the mean absolute deviation of the spectra. Estimates of ε, whose mean absolute deviation were higher than 0.4, were not considered (e.g., McMillan et al., 2016). This parameter is the average absolute deviation between the measured spectrum and the Nasmyth spectrum (Ruddick et al., 2000).

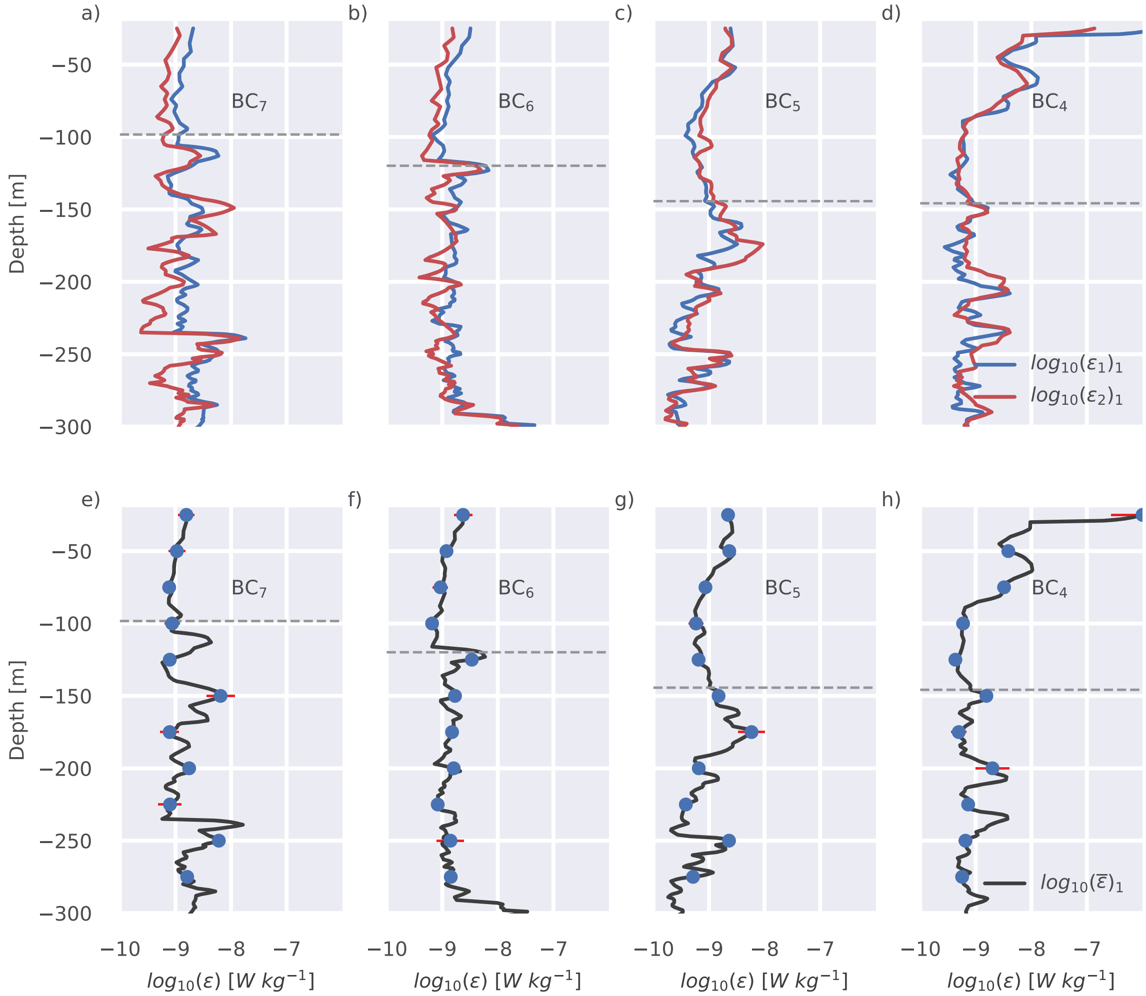

Figure 5. Panels (a)–(d) show the vertical profiles of ε estimated from the shear probe 1 (blue) and 2 (red) from the first cast. Panels (e)–(h) show the average profile of ε from the first cast with its respective error bar every 25 m (blue dots) (standard deviation, solid red line). The horizontal dashed gray lines represent the mixed-layer depth (MLD). The estimates depicted here were calculated with 2-s intervals of the falling-probe in the water column.

The choice of the bin size to determine the highest wavenumber and its respective rate of dissipation of TKE is subjective and dependent on the fall speed of the equipment (1.4 m/s close to the surface and 0.2 m/s at approximately 400 m). Given this subjectivity, a few bin sizes are tested to obtain the best combination of the number of values and reduction of noise. In Figure 4, segments corresponding to 2 s (1–6 m), 4 s (2–11 m), 6 s (3–16 m), and 10 s (3–25 m) are used to convert temporal derivatives to spatial derivatives, assuming a frozen field hypothesis as proposed by Taylor (1938). The smaller the water column segment, the more highly resolved is the TKE dissipation profile, but the greater is the noise carried by the signal (Figure 4). A combination of more highly resolved profiles (Figures 4a–4d) and the small difference between the magnitude of the dissipation rates at the same level (Figures 4e–4h) suggest that ε estimates from a bin size of 2 s provide the best results. Thus, the following results are derived from a bin size of 2 s.

The microstructure profiler is equipped with two shear probes giving duplicates of vertical profiles for each cast. In theory, both shear probes should measure the same microstructures with the same magnitude, though in reality, they present differences due to the sensitivity of each sensor. The contrasts in measurements of dissipation rates of TKE from the respective shear probes can be reduced by using the mean field of TKE dissipation rate estimates (e.g., Doubell et al., 2018). The vertical profiles of ε of each shear probe show a similar vertical distribution of the turbulent motion peaks despite the difference between their magnitudes (Figures 5a–5d). Thus, employing the mean profile is satisfactory for the description of local turbulence (Figures 5e–5h).

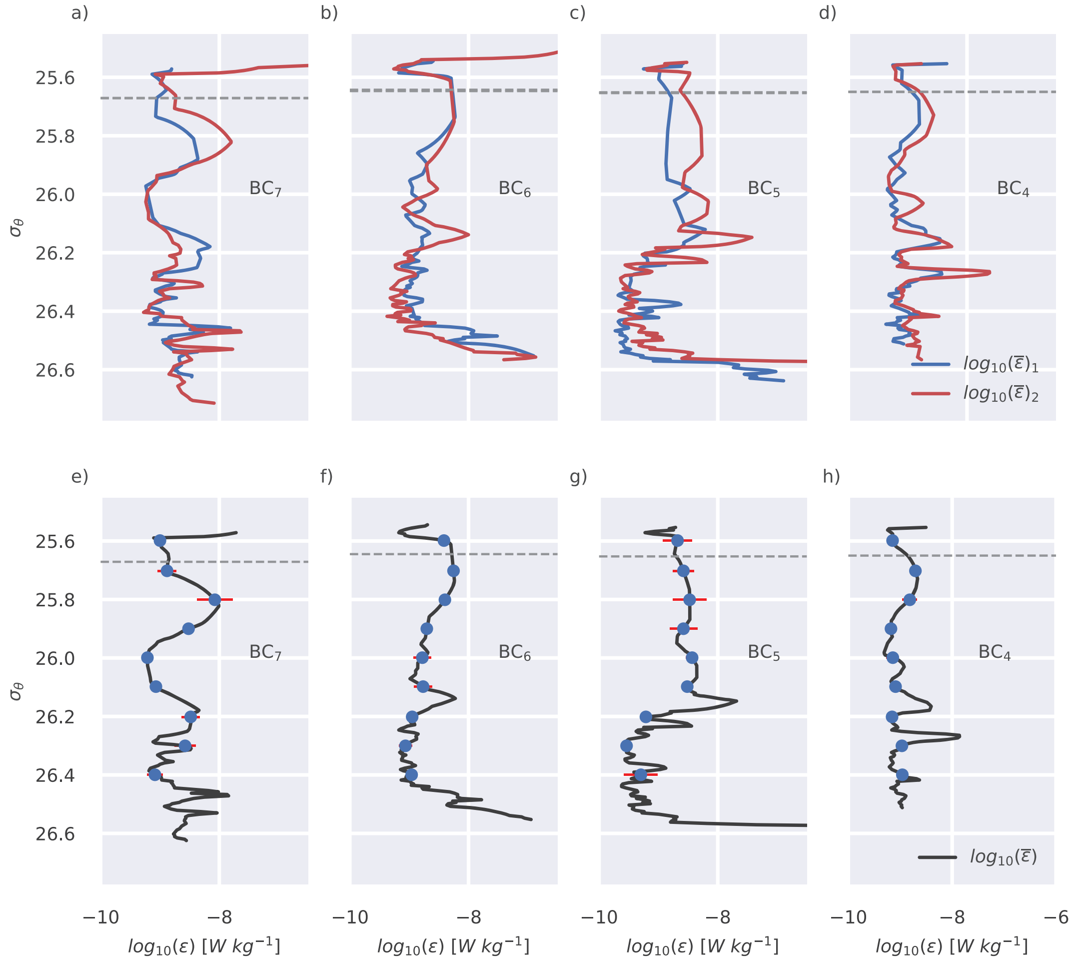

Figure 6. Panels (a)–(d) represent the estimate of the TKE dissipation rates from the average of the first (blue) and second (red) casts; panels (e)–(h) shows the average of ε and density estimate from both casts. The error bar (standard deviation, solid red line) are depicted for every 0.1 kg/m^3 (blue dots). The dashed gray line in all panels represents the density at the MLD.

As mentioned in section 2, two VMP casts were performed at each station, resulting in two averaged profiles separated by approximately 30 min. This time interval is small compared to the turbulent time scale following the equation:

$$\tau = T_{KH}(\partial v/\partial z), \tag{7}$$

where τ and T_{KH} represent the nondimensional and dimensional Kelvin-Helmholtz billow evolution timescales, respectively, and $\partial v/\partial z$ is the Acoustic Doppler Current Profiler cross-transect velocity vertical shear (MacDonald & Chen, 2012). The Kelvin-Helmholtz billow evolution timescales from the BC-IWBC are on the order of hours ($T_{KH_{min}}$ = 45 min at the most sheared layer). Stationary turbulence could be expected, since the reverse flow is geostrophic. Thus, both casts are measuring the same turbulent feature, although peaks of ε may occur with a slight difference in depths at the same station. To avoid capturing peaks of ε at different depths due to the heaving of isopycnals—to filter the internal-wave signal—, ε is interpolated into an isopycnal coordinate (Figure 6). Now, peaks of ε appear at the same density range in both casts at each station, allowing the computation of the averaged profile of both casts, which is assumed to be a reasonable measure of the TKE dissipation rate at each station.

The composite mean of TKE dissipation rate at each oceanographic station shows thin subsurface patches of O(10^{-8}) W/kg with background values of O(10^{-10}) W/kg (Figure 7). Two (sometimes three) marked patches of ε are well defined at each station. The first TKE dissipation rate peaks occur at the level of the SML depth and just below it. At station BC_7, the first peak reaches O(10^{-8}) W/kg following the highest stratification that

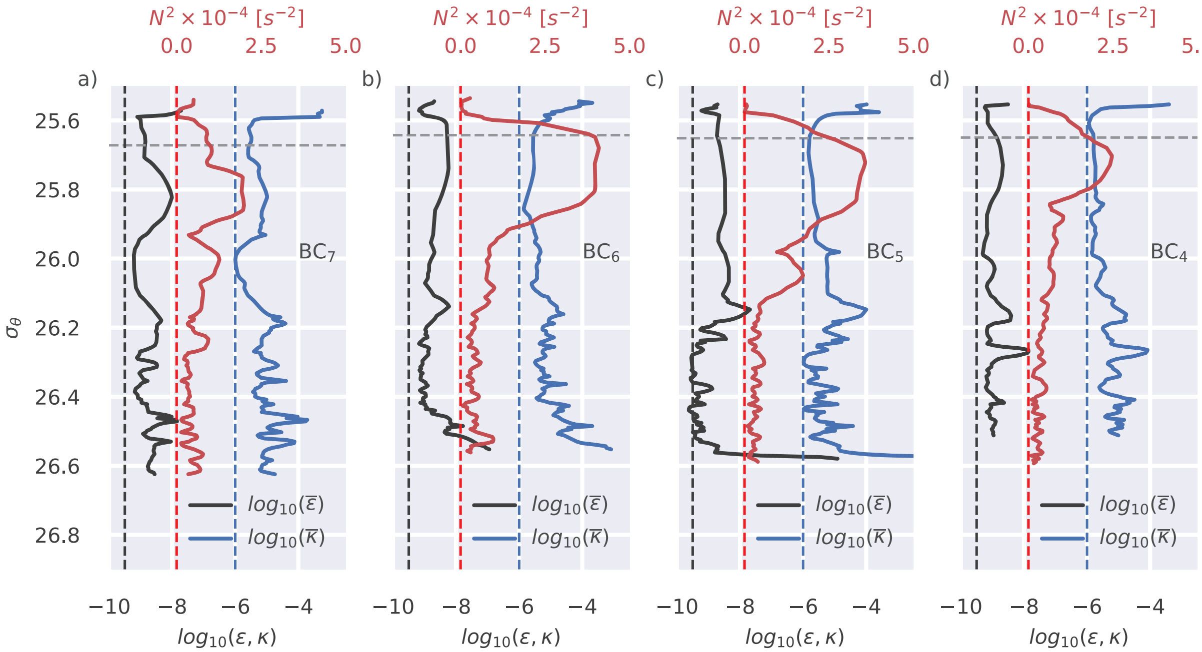

Figure 7. Vertical profiles of TKE dissipation rates (solid black lines), vertical diffusivity profiles (solid blue lines), and stratification profiles (solid red lines). Dashed gray, red, black, and blue lines represent the density at the MLD, the zero of the stratification ($N^2 = 0$), the background value for TKE dissipation rates, and the background value for vertical diffusivity, respectively.

occurs about 10 m below the lower limit of the SML, between 1,025.7 and 1,025.9 kg/m^3. The second peak of energy dissipation rate at station BC_7 reaches O(10^{-9}) W/kg and occurs between 1,026.1 and 1,026.3 kg/m^3 at approximately 150 m. At the other three stations (BC_6, BC_5, and BC_4) (Figure 7), the first peak of ε at each station is at the same density interval as the SML depth, and the second peak occurs also between 1,026.1 and 1,026.3 kg/m^3. It is important to note that the base of the SML (peaks of ε) gets deeper in the offshore direction (Figure 5), following the stronger signals of vertical shear (stratification) (Figure 2). As the stratification becomes weaker below the SML, the magnitude of the vertical shear becomes stronger between 70 and 160 m in the western portion of the section and between 120 and 250 m in the eastern portion of the section. In turn, the zonal variation of the depth of greater vertical shear coincides with the depth of the BC and IWBC inversion.

In summary, the upper peaks of TKE dissipation rate coexist with strong stratification below the SML in the BC-IWBC domain (Figure 7). On the other hand, lower peaks of TKE dissipation rate are generally in the region of lower stratification but more intense shear due to the reversal flow. This relationship highlights the role of vertical shear in developing turbulent motions within the interface between the BC and the IWBC. Thus, small-scale processes at the pycnocline may generate turbulent mixing and provide exchanges of properties between the salty and nitrate-poor surface water and the fresher and nutrient-rich subsurface water mass of the western South Atlantic.

4.2. Mixing and Turbulent Vertical Fluxes

A turbulent flow is diffusive and dissipative, which means that there is rapid mixing of fluid properties and kinetic energy is irreversibly lost through friction (Thorpe, 2007). The magnitude of the diffusivity in the interior ocean affects a wide range of processes, from the dispersion of nonconservative properties such as nutrients to the vertical transport of salt and heat, affecting ultimately the stratification of the water column. To verify whether or not the subsurface turbulence in the BC-IWBC domain may drive mixing processes at the interface of these two jets, the Osborn model (Osborn, 1980) is used to compute the vertical diffusivity (e.g., Doubell et al., 2018; Itoh et al., 2010; Kaneko et al., 2013):

$$\kappa_\rho = \Gamma \frac{\varepsilon}{N^2}, \tag{8}$$

where $\Gamma = 0.2$ is the mixing efficiency parameter (Gregg et al., 2018; Imberger & Ivey, 1991). Turbulent diffusivity was also expressed in terms of the turbulence activity parameter ($\varepsilon / \nu N^2$), which exhibits a linear relationship at the stationary and intermediate turbulence regime (Shih et al., 2005).

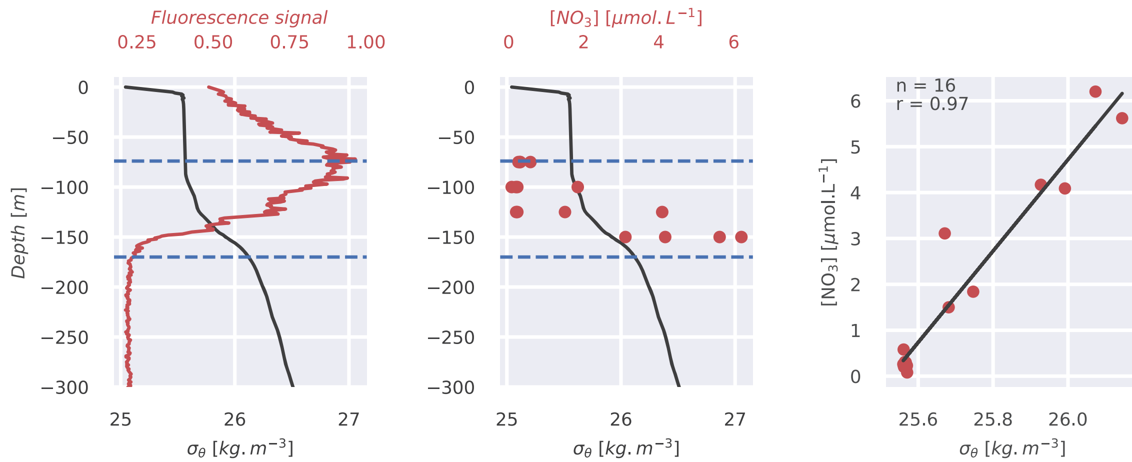

Figure 8. (a and b) The average density profiles (black) and the fluorescence signal from the CTD (red). Blue dashed horizontal lines delimit the lower half of the maximum fluorescence subsurface. Red dots represent the concentrations of nitrate. (c) shows the scatter plot of the nitrate and density samples and its linear regression.

Figure 7 shows that κ_ρ values within the SML are of O(10^{-4}) m^2/s. These values decrease below the SML depth, where high stratification creates a physical barrier to vertical exchanges. Like the vertical distribution of TKE dissipation rates, peaks of vertical diffusivities, higher than the background values, are observed at the pycnocline. However, even with strong stratification, an intense relative vertical diffusivity O(10^{-5}) m^2/s is observed at station BC$_7$ at density surfaces below the SML (Figure 7a). Below the pycnocline, multiple peaks of strong diffusivity are observed with orders of magnitude higher than the background, particularly close to the isopycnal 1,026.2 kg/m^3, where a burst of turbulence is observed. According to the turbulence activity parameter, the intermediate regime of turbulence dominates between the base of the SML and the 1,026.2 isopycnals (not shown). At those depths, vigorous patches of κ_ρ play an important role in the turbulent flux of conservative and nonconservative properties, which can be estimated from

$$F_c = -\kappa_\rho \frac{\partial C}{\partial z}, \tag{9}$$

where $\partial C/\partial z$ is the vertical gradient of a scalar property C (e.g., Doubell et al., 2018; Kaneko et al., 2013; Rumyantseva et al., 2015).

Based on the higher values of turbulence observed below the SML, which are caused by the interaction of the nitrate-poor BC with the nitrate-rich IWBC, high levels of mixing and property exchange are expected near and below the pycnocline. Thus, we hypothesize that mixing at the interface of BC-IWBC may bring new nutrients (NO$_3$) to the upper ocean, promoting an increase in new production. To test this hypothesis, an estimate of the vertical turbulent nitrate flux (F_{NO_3}) was conducted based on equation (9). As the VMP was not equipped with a nitrate profiler, a density-nitrate relationship was built using the hydrographic data from the CTD and water samples from Niskin bottles for the lower half of the chlorophyll-a fluorescence maximum signal (Figure 8a). Chlorophyll-a fluorescence is the most commonly used index of phytoplankton biomass which is controlled primarily by the nutrient (nitrate) transport within the ocean (Sarmiento & Gruber, 2006). The density-nitrate relationship was applied to the microstructure-derived density to estimate the microscale vertical distribution of nitrate (e.g., Rumyantseva et al., 2015; Sharples et al., 2007). One advantage of having a reliable density-nitrate relationship is that measurements of the nitrate gradient and turbulent diffusivity can be obtained via the same instrument at the same time. This avoids the uncertainties associated with spatiotemporal differences that arise when the turbulent diffusivity and the nitrate gradient are obtained through different releases (Sharples et al., 2001, 2007). Following Sharples et al. (2007), Figure 8 shows the vertical level of the nitrate samples used to build the linear density-nitrate relationship. Using equation (9) and the microstructure-derived density data, the nitrate flux is estimated as

$$F_{NO_3} = -\kappa_\rho \frac{\partial NO_3(\rho)}{\partial z}. \tag{10}$$

Negative vertical gradients of nitrate appear throughout the whole water column. A prominent vertical gradient occurs between the SML depth and the isopycnal 1,025.7 kg/m^3, which marks the upper level of the

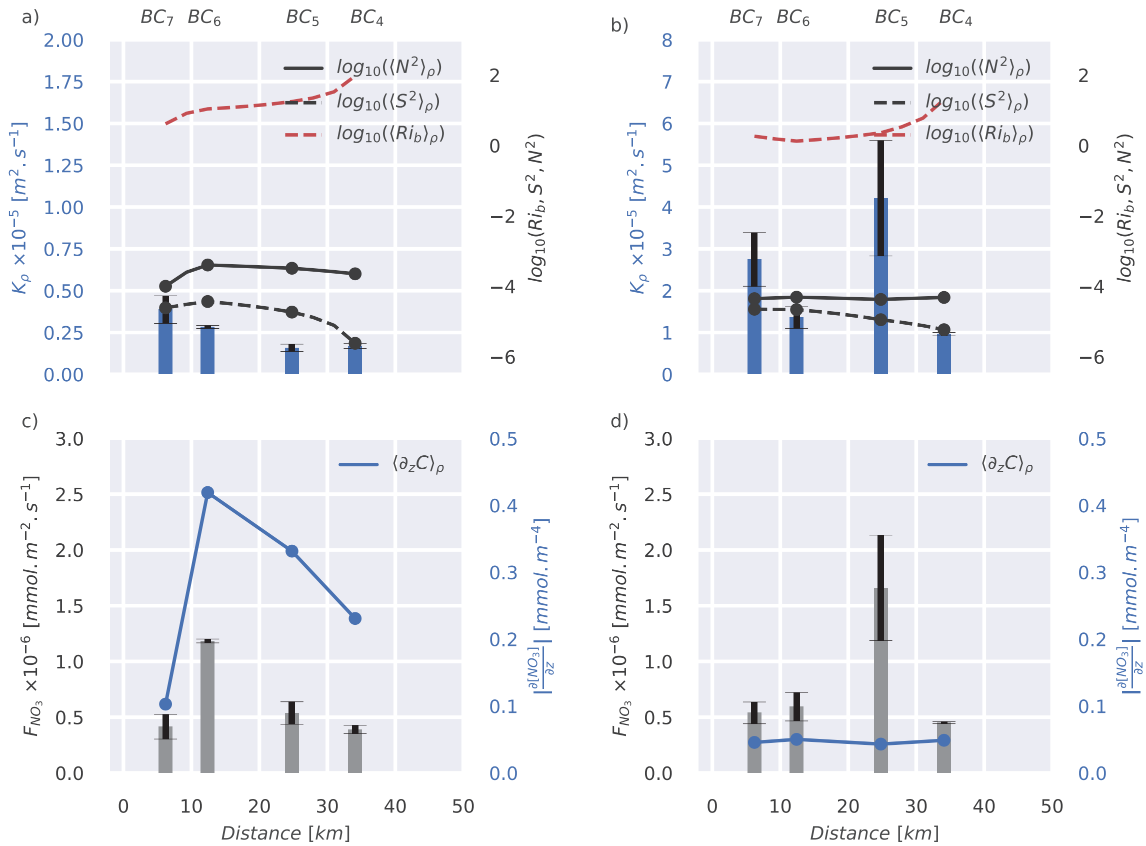

Figure 9. Vertical diffusivity (a, b) and turbulent nitrate flux (c, d) at pycnoclinic (a, c) and subpycnoclinic (b, d) levels. Blue bars in panels (a) and (b) represent the mean values of the vertical diffusivity between isopycnals of 1,025.65–1,025.75 kg/m^3 (left) and 1,026.1–1,026.2 kg/m^3 (right), while gray bars in panels (c) and (d) represent the mean of the vertical turbulent nitrate flux in the same intervals of density. Vertical black lines are the standard deviation of its respective quantities. Dashed red and black lines represent the zonal variation of Ri_b, and the vertical shear intensity, respectively. Solid black and blue lines represent the buoyancy frequency and vertical nitrate gradient, respectively. The bars represent stations BC_7, BC_6, BC_5, and BC_4, as indicated in the top.

nitrate-rich subsurface water mass (Stramma & England, 1999). The value of the F_{NO_3} is estimated from the average of each quantity in equation (10) along the isopycnals that presented the highest peaks of turbulence. Figures 9a and 9c show the average of these quantities, as well as the average of N^2 and S^2 in the form of the bulk Richardson number (Ri_b)

$$Ri_b = \frac{\langle N^2\rangle_\rho}{\langle S^2\rangle_\rho}, \tag{11}$$

where $\langle \cdot \rangle_\rho$ denotes the average between the 1,025.65- and 1,025.75-kg/m^3 isopycnals. Shear (stratification) becomes weaker (stronger) in the offshore direction. The relation between the magnitudes of these two terms becomes clear when we look at the zonal variation of the Ri_b, which shows greater susceptibility to the development of instabilities in the stations to the west (Figure 9a). This pattern is followed by the magnitude of the vertical diffusivity, with higher values in the western portion of the section, resulting in more mixing. Westernmost stations are closer to the BC core—which contains the highest-shear layer, trapped between the SML depth and the zero isotach. Moreover, the nitrate gradient shows a maximum at station BC$_6$, producing a more intense turbulent flux (Figure 9c). Figures 9b and 9d show the average of terms of equations (10) and (11) for the density range of 1,026.1 to 1,026.2 kg/m^3, corresponding to the maximum dissipation of TKE. The variations in the average N^2 and S^2 are more subtle at the subpycnoclinic levels than at the pycnoclinic levels; that is, while the stratification remains approximately constant over the section, the vertical shear shows a slight decrease in its intensity in the offshore direction. On average, the Ri_b below the pycnocline is lower than the Ri_b into the SML depth triggering shear instability, which in turn results in the strong vertical diffusivities at these density levels. In this case, the vertical nitrate gradient values were minimal, resulting in the pattern of zonal variation of the turbulent flux being similar to that of the diffusivity rates. Despite the

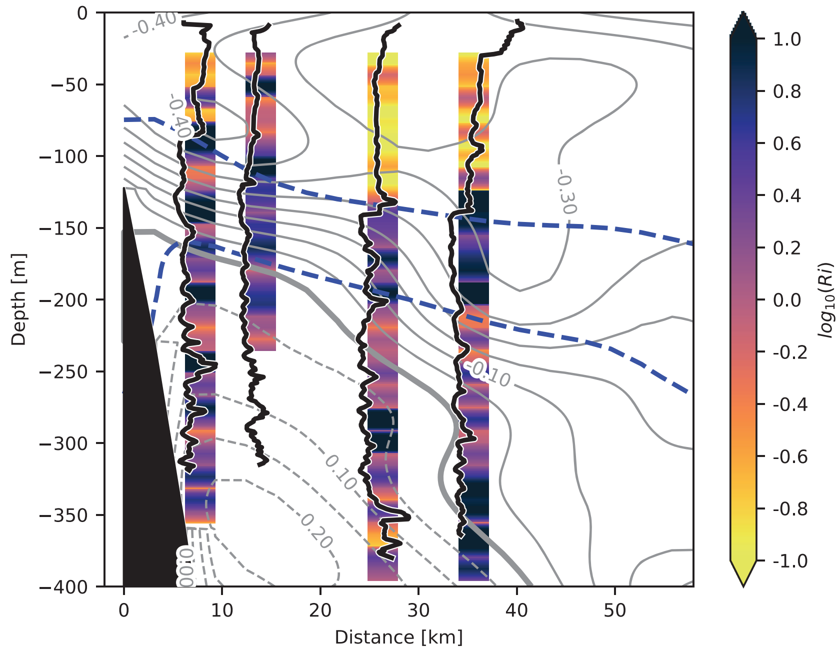

Figure 10. The background color represents the 8-m Richardson number (*Ri*) with gray contours of negative (solid lines) and positive (dashed lines) isotachs. Dashed blue lines represent the isopycnals of the base of the SML (upper) and the isopycnal of 1,026.2 kg/m^3 (lower). Black lines represent the vertical profiles of the vertical diffusivity on logarithmic scale.

small gradient of nitrate at deeper levels, the deep turbulent flux has the same magnitude of those acting on the main source of nitrate—the subsurface water—and in the lower limit of the SML.

5. Discussion and Concluding Remarks

In this study, microscale measurements in a region of interaction between the mutually opposing flows of two western boundary currents in the southwestern Atlantic Ocean are used to explore the role of the vertical shear on the mixing processes and nitrate exchange. Shear instabilities analyzed from vertical microstructure observations below the SML may drive an intense turbulent mixing activity, possibly supplying the upper ocean with new nutrients.

Instabilities of the upper ocean may occur on more refined horizontal scales (Mahadevan & Tandon, 2006) than that captured by the measurements during the BC-IWBC mixing experiment. However, at the measured scale, the destabilizing influence of the BC-IWBC shear overcomes the stabilizing stratification influence ($Ri \leq 1$). This tendency is further supported by the destabilizing effect of the baroclinicity. To evaluate the unstable water column motion further, horizontal high-resolution in situ data are required as well as the sampling of meridional variations of quantities assumed to be negligible in the present study. Nevertheless, previous studies conducted by Silveira et al. (2008) and Rocha et al. (2014) suggest that the BC-IWBC is baroclinically unstable. The flow structure measured in our section satisfies the baroclinic instability criterion, and in addition, the microstructure also shows that shear instability may also occur within the BC-IWBC system at finer vertical scales.

Instabilities in the upper ocean have an important role in the global energy budget, maintaining small-scale processes by the forward energy cascade. In the BC-IWBC mixing experiment, enhanced turbulent motions were observed at the isopycnals within the lower limit of the SML and underneath it. There, high vertical shear may erode strong stratification, resulting in a relevant peak of turbulence. According to Whitt and Taylor (2017), dissipation rates may remain elevated throughout the strong mean stratification and have important implications for the energy budget. Due to the attachment of the cores of the BC and the IWBC to the continental slope (Silveira et al., 2004), it is possible to see the zonal variation in depth of the turbulence signal, following enhanced vertical shear and the stratified layer as well as the SML depth (Figure 10).

Nonetheless, weaker stratification below the pycnocline combined with more intense vertical shear suggests greater mixing and potential for exchange of properties.

Maximum values of vertical diffusivity of O(10^{-4}) m^2/s were observed trapped in the SML by the high stratification in the lower SML. Moreover, values of O(10^{-5}) m^2/s were observed below the pycnocline (Figure 7). This pattern agrees well with those obtained by Dunckley et al. (2012), who tested different models for estimating vertical diffusivities. One of the most important points of the present study is the verification of strong vertical diffusivity occurring below the SML. Peaks of 1 order of magnitude higher than the background values emphasize the importance of the vertical shear under the weakly stratified condition. This relationship becomes clear when we observe the zonal variation of turbulent diffusive processes, which agrees well with the Ri_b variation, evidencing the propensity of the flow to develop shear instabilities linked to the BC-IWBC interaction. The shear at the interface of this system may also be enhanced through internal waves (e.g., Pereira et al., 2005). However, further studies should be conducted to reveal their role in producing turbulence since the observed amount of turbulence indicates stationary turbulence. Small-scale turbulence is an ubiquitous feature on the residual layer and is also shown to exist in regions with significantly larger Ri (Balsley et al., 2008). However, due to relatively weak mixing at the isopycnal of the base of the SML, vertical turbulent nitrate flux occurs in a less expressive way, even in the presence of a stronger nitrate vertical gradient (Figure 9). Even with relatively weak mixing below the SML, it has the potential to bring nitrate to the upper layer. This implies a potential enhancement in primary productivity within an oligotrophic region. The magnitude of the nitrate flux observed in the present study is the same as that noted at the Great Australia Bight (Doubell et al., 2018) and in the southern side of Kuroshio front where low nitrate gradient was also observed (Kaneko et al., 2013). This mechanism can also be enhanced by the passage of an atmospheric system (Rumyantseva et al., 2015; Thomas et al., 2016), as well as by the net seasonal heat flux variability, not discussed in the present study.

Intense mixing near and below the pycnocline enhance turbulent fluxes and hence increase the upward supply of nutrients. However, unlike high nitrate vertical gradients close to the base of the SML, low nitrate gradients in deeper levels show comparable turbulent nitrate flux driven by the more intense mixing due to the BC-IWBC system. These deeper fluxes could prove more important with photosynthetically active radiation reaching these depths and should be investigated in future studies.

Acknowledgments

C. Z. Lazaneo acknowledges support from Coordenação de Aperfeiçoamento de Pessoal de Nível Superior-Brasil (CAPES)-Finance Code 001 and from Conselho Nacional de Desenvolvimento Científico e Tecnológico - CNPq (Processo 205857/2018-3). I. C. A. da Silveira acknowledges support from CNPq (Grant 307814/2017-3), Projeto SUBMESO (Processo CNPq 442926/2015-4), Projeto REMARSUL (Processo CAPES 88882.158621/2014-01), and Projeto VT-Dyn (Processo FAPESP 2015/21729-4). A. Tandon acknowledges support from NSF Grants OCE1434512, OCE1558849, and OCE1755313. P. H. R. Calil acknowledges support from Projeto ILHAS (Processo CNPq 458583/2013-8). The authors are very grateful to the crew of *R/V Alpha Crucis* and, in particular, Captain Jos H. M. Rezende. C. Z. Lazaneo is grateful to Justine McMillan (Rockland Scientific) for her help with the microstructure data processing. We sincerely thank the anonymous Reviewer's for their comments which helped improve and clarify this manuscript. The data analyzed in this study can be obtained at the website (https://jmp.sh/72IEgOV).

References

Balsley, B. B., Svensson, G., & Tjernström, M. (2008). On the scale-dependence of the gradient Richardson number in the residual layer. *Boundary-Layer Meteorology*, *127*(1), 52–72. https://doi.org/10.1007/s10546-007-9251-0

Boccaletti, G., Ferrari, R., & Fox-Kemper, B. (2007). Mixed layer instabilities and restratification. *Journal of Physical Oceanography*, *37*(9), 2228–2250. https://doi.org/10.1175/JPO3101.1

Boebel, O., Davis, R. E., Ollitrault, M., Peterson, R. G., Richardson, P. L., Schmid, C., & Zenk, W. (1999). The intermediate depth circulation of the western South Atlantic. *Geophysical Research Letters*, *26*(21), 3329–3332. https://doi.org/10.1029/1999GL002355

D'Asaro, E., Lee, C., Thomas, L., & Harcourt, R. (2011). Enhanced turbulence and energy dissipation at ocean fronts. *Science*, *332*(6027), 318–322. https://doi.org/10.1126/science.1201515

de Boyer Montégut, C., Madec, G., Fischer, A. S., Lazar, A., & Iudicone, D. (2004). Mixed layer depth over the global ocean: An examination of profile data and a profile-based climatology. *Journal of Geophysical Research*, *109*, C12003. https://doi.org/10.1029/2004JC002378

Doubell, M. J., Spencer, D., van Ruth, P. D., Lemckert, C., & Middleton, J. F. (2018). Observations of vertical turbulent nitrate flux during summer in the Great Australian Bight. *Deep-Sea Research Part II: Topical Studies in Oceanography*, *157*, 27–35. https://doi.org/10.1016/j.dsr2.2018.08.007

Dunckley, J. F., Koseff, J. R., Steinbuck, J. V., Monismith, S. G., & Genin, A. (2012). Comparison of mixing efficiency and vertical diffusivity models from temperature microstructure. *Journal of Geophysical Research*, *117*, C10008. https://doi.org/10.1029/2012JC007967

Ferrari, R., & Wunsch, C. (2009). Ocean circulation kinetic energy: Reservoirs, sources, and sinks. *Annual Review of Fluid Mechanics*, *41*(1), 253–282. https://doi.org/10.1146/annurev.fluid.40.111406.102139

Firing, E. (1995). Processing ADCP data with the CODAS software system version 3.1. Joint Institute for Marine and Atmospheric Research, University of Hawaii & National Oceanographic Data Center.

Gargett, A. E. (1997). "Theories" and techniques for observing turbulence in the ocean euphotic zone. *Scientia Marina*, *61*, 25–45.

Grasshoff, K., Kremling, K., & Ehrhardt, M. (2009). *Methods of seawater analysis*. New York: John Wiley.

Gregg, M. C. (1987). Diapycnal mixing in the thermocline: A review. *Journal of Geophysical Research*, *92*(C5), 5249–5286. https://doi.org/10.1029/JC092iC05p05249

Gregg, M. C. (1989). Scaling turbulent dissipation in the thermocline. *Journal of Geophysical Research*, *94*(C7), 9686. https://doi.org/10.1029/jc094ic07p09686

Gregg, M. C. (1999). Uncertainties and limitations in measuring ε and χ T. *Journal of Atmospheric and Oceanic Technology*, *16*(11), 1483–1490. https://doi.org/10.1175/1520-0426(1999)016<1483:UALIMA>2.0.CO;2

Gregg, M. C., D'Asaro, E. A., Riley, J. J., & Kunze, E (2018). Mixing efficiency in the ocean. *Annual Review of Marine Science*, *10*(1), 443–473. https://doi.org/10.1146/annurev-marine-121916-063643

Hoskins, B. J. (1974). The role of potential vorticity in symmetric stability and instability. *Quarterly Journal of the Royal Meteorological Society*, *100*(425), 480–482. https://doi.org/10.1002/qj.49710042520

Hoskins, B. J., & Bretherton, F. P. (1972). Atmospheric frontogenesis models: Mathematical formulation and solution. *Journal of the Atmospheric Sciences*, *29*, 11–37. https://doi.org/10.1175/1520-0469(1972)029<0011:AFMMFA>2.0.CO;2

Imberger, J., & Ivey, G. N. (1991). On the nature of turbulence in a stratified fluid. Part II: Application to lakes. *Journal of Physical Oceanography*, *21*(5), 659–680. https://doi.org/10.1175/1520-0485(1991)021<0659:otnoti>2.0.co;2

Itoh, S., Yasuda, I., Nakatsuka, T., Nishioka, J., & Volkov, Y. N. (2010). Fine- and microstructure observations in the Urup Strait, Kuril Islands, during August 2006. *Journal of Geophysical Research*, *115*, 8004. https://doi.org/10.1029/2009JC005629

Kaneko, H., Yasuda, I., Komatsu, K., & Itoh, S. (2012). Observations of the structure of turbulent mixing across the Kuroshio. *Geophysical Research Letters*, *39*, L15602. https://doi.org/10.1029/2012GL052419

Kaneko, H., Yasuda, I., Komatsu, K., & Itoh, S. (2013). Observations of vertical turbulent nitrate flux across the Kuroshio. *Geophysical Research Letters*, *40*, 3123–3127. https://doi.org/10.1002/grl.50613

Kolmogorov, A. N. (1968). Local structure of turbulence in an incompressible viscous fluid at very high Reynolds numbers. *Soviet Physics Uspekhi*, *10*(6), 734–746. https://doi.org/10.1070/PU1968v010n06ABEH003710

Kunze, E., Firing, E., Hummon, J. M., Chereskin, T. K., & Thurnherr, A. M. (2006). Global abyssal mixing inferred from lowered ADCP shear and CTD strain profiles. *Journal of Physical Oceanography*, *36*(8), 1553–1576. https://doi.org/10.1175/jpo2926.1

Ledwell, J. R., Montgomery, E. T., Polzin, K. L., Laurent, L. C. S., Schmitt, R. W., & Toole, J. M. (2000). Evidence for enhanced mixing over rough topography in the abyssal ocean. *Nature*, *403*(6766), 179–182. https://doi.org/10.1038/35003164

Lueck, R. G., Crawford, W. R., & Osborn, T. R. (1983). Turbulent dissipation over the continental slope off Vancouver Island. *Journal of Physical Oceanography*, *13*(10), 1809–1818. https://doi.org/10.1175/1520-0485(1983)013<1809:tdotcs>2.0.co;2

MacDonald, D. G., Carlson, J., & Goodman, L. (2013). On the heterogeneity of stratified-shear turbulence: Observations from a near-field river plume. *Journal of Geophysical Research: Oceans*, *118*, 6223–6237. https://doi.org/10.1002/2013JC008891

MacDonald, D. G., & Chen, F. (2012). Enhancement of turbulence through lateral spreading in a stratified-shear flow: Development and assessment of a conceptual model. *Journal of Geophysical Research*, *117*, C05025. https://doi.org/10.1029/2011JC007484

Mahadevan, A., & Tandon, A. (2006). An analysis of mechanisms for submesoscale vertical motion at ocean fronts. *Ocean Modelling*, *14*(3-4), 241–256. https://doi.org/10.1016/j.ocemod.2006.05.006

Mahadevan, A., Tandon, A., & Ferrari, R. (2010). Rapid changes in mixed layer stratification driven by submesoscale instabilities and winds. *Journal of Geophysical Research*, *115*, C03017. https://doi.org/10.1029/2008JC005203

McMillan, J. M., Hay, A. E., Lueck, R. G., & Wolk, F. (2016). Rates of dissipation of turbulent kinetic energy in a high reynolds number tidal channel. *Journal of Atmospheric and Oceanic Technology*, *33*(4), 817–837. https://doi.org/10.1175/JTECH-D-15-0167.1

McWilliams, J. C. (2016). Submesoscale currents in the ocean (Vol. 472) (No. 2189). https://doi.org/10.1098/rspa.2016.0117

Miles, J. W. (1961). On the stability of heterogeneous shear flows. *Journal of Fluid Mechanics*, *10*(4), 496–508. https://doi.org/10.1017/S0022112061000305

Molemaker, M. J., McWilliams, J. C., & Capet, X. (2010). Balanced and unbalanced routes to dissipation in an equilibrated Eady flow. *Journal of Fluid Mechanics*, *654*, 35–63. https://doi.org/10.1017/S0022112009993272

Moum, J. N., & Osborn, T. R. (1986). Mixing in the main thermocline. *Journal of Physical Oceanography*, *16*(7), 1250–1259. https://doi.org/10.1175/1520-0485(1986)016<1250:mitmt>2.0.co;2

Munk, W., & Wunsch, C. (1998). Abyssal recipes II: Energetics of tidal and wind mixing. *Deep Sea Research Part I: Oceanographic Research Papers*, *45*(12), 1977–2010.

Nagai, T., Tandon, A., Gruber, N., & McWilliams, J. C. (2008). Biological and physical impacts of ageostrophic frontal circulations driven by confluent flow and vertical mixing. *Dynamics of Atmospheres and Oceans*, *45*(3-4), 229–251. https://doi.org/10.1016/j.dynatmoce.2007.12.001

Nagai, T., Tandon, A., Yamazaki, H., & Doubell, M. J. (2009). Evidence of enhanced turbulent dissipation in the frontogenetic Kuroshio Front thermocline. *Geophysical Research Letters*, *36*, L12609. https://doi.org/10.1029/2009GL038832

Nikurashin, M., & Ferrari, R. (2011). Global energy conversion rate from geostrophic flows into internal lee waves in the deep ocean. *Geophysical Research Letters*, *38*, L08610. https://doi.org/10.1029/2011GL046576

Nikurashin, M., Vallis, G. K., & Adcroft, A. (2013). Routes to energy dissipation for geostrophic flows in the Southern Ocean. *Nature Geoscience*, *6*(1), 48–51. https://doi.org/10.1038/ngeo1657

Oakey, N. S. (1982). Determination of the rate of dissipation of turbulent energy from simultaneous temperature and velocity shear microstructure measurements. *Journal of Physical Oceanography*, *12*(3), 256–271. https://doi.org/10.1175/1520-0485(1982)012<0256:dotrod>2.0.co;2

Osborn, T. R. (1980). Estimates of the local rate of vertical diffusion from dissipation measurements. *Journal of Physical Oceanography*, *10*(1), 83–89. https://doi.org/10.1175/1520-0485(1980)010<0083:eotlro>2.0.co;2

Pereira, A. F., Belém, A. L., Castro, B. M., & Geremias, R. (2005). Tidetopography interaction along the eastern Brazilian shelf. *Continental Shelf Research*, *25*(12-13), 1521–1539. https://doi.org/10.1016/j.csr.2005.04.008

Polzin, K. L., Toole, J. M., Ledwell, J. R., & Schmitt, R. W. (1997). Estimates of diapycnal mixing in the abyssal ocean. *Science*, *276*(5309), 93–96. https://doi.org/10.1126/science.264.5162.1120

Ramachandran, S., Tandon, A., Mackinnon, J., Lucas, A. J., Pinkel, R., Waterhouse, A. F., et al. (2018). Submesoscale processes at shallow salinity fronts in the Bay of Bengal: Observations during the winter monsoon. *Journal of Physical Oceanography*, *48*(3), 479–509. https://doi.org/10.1175/jpo-d-16-0283.1

Rocha, C. B., da Silveira, I. C., Castro, B. M., & Lima, J. A. M. (2014). Vertical structure, energetics, and dynamics of the Brazil Current System at 22°S–28°S. *Journal of Geophysical Research: Oceans*, *119*, 52–69. https://doi.org/10.1002/2013JC009143

Ruddick, B., Anis, A., & Thompson, K. (2000). Maximum likelihood spectral fitting: The batchelor spectrum. *Journal of Atmospheric and Oceanic Technology*, *17*(11), 1541–1555. https://doi.org/10.1175/1520-0426(2000)017<1541:MLSFTB>2.0.CO;2

Rumyantseva, A., Lucas, N., Rippeth, T., Martin, A., Painter, S. C., Boyd, T. J., & Henson, S. (2015). Ocean nutrient pathways associated with the passage of a storm. *Global Biogeochemical Cycles*, *29*, 1179–1189. https://doi.org/10.1002/2015GB005097

Sarmiento, J. L., & Gruber, N. (2006). *Ocean biogeochemical dynamics*. Princeton: Princeton University Press.

Sharples, J., Moore, C. M., Rippeth, T. P., Holligan, P. M., Hydes, D. J., Fisher, N. R., & Simpson, J. H. (2001). Phytoplankton distribution and survival in the thermocline. *Limnology and Oceanography*, *46*(3), 486–496. https://doi.org/10.4319/lo.2001.46.3.0486

Sharples, J., Tweddle, J. F., Green, J. A. M., Palmer, M. R., Kim, Y. N., Hickman, A. E., et al. (2007). Spring-neap modulation of internal tide mixing and vertical nitrate fluxes at a shelf edge in summer. *Limnology and Oceanography*, *52*(5), 1735–1747. https://doi.org/10.4319/lo.2007.52.5.1735

Shih, L. H., Koseff, J. R., Ivey, G. N., & Ferziger, J. H. (2005). Parameterization of turbulent fluxes and scales using homogeneous sheared stably stratified turbulence simulations. *Journal of Fluid Mechanics*, *525*, 193–214. https://doi.org/10.1017/S0022112004002587

Silveira, I. C. A., Calado, L., Castro, B. M., Cirano, M., Lima, J. A. M., & Mascarenhas, A. d. S. (2004). On the baroclinic structure of the Brazil Current-Intermediate Western Boundary Current system at 22°–23°S. *Geophysical Research Letters*, *31*, L14308. https://doi.org/10.1029/2004GL020036

Silveira, I. C. A., Lima, J. A. M., Schmidt, A. C. K., Ceccopieri, W., Sartori, A., Franscisco, C. P. F., & Fontes, R. F. C. (2008). Is the meander growth in the Brazil Current system off Southeast Brazil due to baroclinic instability? *Dynamics of Atmospheres and Oceans*, *45*(3-4), 187–207. https://doi.org/10.1016/j.dynatmoce.2008.01.002

Smith, W. H., & Sandwell, D. T. (1997). Global sea floor topography from satellite altimetry and ship depth soundings. *Science*, *277*(5334), 1956–1962. https://doi.org/10.1126/science.277.5334.1956

Soutelino, R. G., Silveira, I. C. A., Gangopadhyay, A., & Miranda, J. A. (2011). Is the Brazil Current eddy-dominated to the north of 20°S? *Geophysical Research Letters*, *38*, L03607. https://doi.org/10.1029/2010GL046276

Stramma, L., & England, M. (1999). On the water masses and mean circulation of the South Atlantic Ocean. *Journal of Geophysical Research*, *104*(C9), 20,863–20,883. https://doi.org/10.1029/1999jc900139

Taylor, G. I. (1938). The spectrum of turbulence. *Proceedings of the Royal Society of London. Series A-Mathematical and Physical Sciences*, *164*(919), 476–490. https://doi.org/10.2514/8.1235

Taylor, J. R., & Ferrari, R. (2009). On the equilibration of a symmetrically unstable front via a secondary shear instability. *Journal of Fluid Mechanics*, *622*, 103–113. https://doi.org/10.1017/S0022112008005272

Thomas, L. N., Tandon, A., & Mahadevan, A. (2008). Submesoscale processes and dynamics. *Geophysical Monograph Series*, *177*, 17–38. https://doi.org/10.1029/177GM04

Thomas, L. N., Taylor, J. R., D'Asaro, E. A., Lee, C. M., Klymak, J. M., & Shcherbina, A. (2016). Symmetric instability, inertial oscillations, and turbulence at the Gulf Stream Front. *Journal of Physical Oceanography*, *46*, 197–217. https://doi.org/10.1175/jpo-d-15-0008.1

Thomas, L. N., Taylor, J. R., Ferrari, R., & Joyce, T. M. (2013). Symmetric instability in the Gulf Stream. *Deep-Sea Research Part II: Topical Studies in Oceanography*, *91*, 96–110. https://doi.org/10.1016/j.dsr2.2013.02.025

Thorpe, S. A. (1973). Experiments on instability and turbulence in a stratified shear flow. *Journal of Fluid Mechanics*, *61*(4), 731–751. https://doi.org/10.1017/S0022112073000911

Thorpe, S. A. (2007). *An introduction to ocean turbulence*. Cambridge: Cambridge University Press.

Whitt, D. B., & Taylor, J. R. (2017). Energetic submesoscales maintain strong mixed layer stratification during an autumn storm. *Journal of Physical Oceanography*, *47*(10), 2419–2427. https://doi.org/10.1175/jpo-d-17-0130.1

Wolk, F., Yamazaki, H., Seuront, L., & Lueck, R. G. (2002). A new free-fall profiler for measuring biophysical microstructure. *Journal of Atmospheric and Oceanic Technology*, *19*(5), 780–793. https://doi.org/10.1175/1520-0426(2002)019<0780:ANFFPF>2.0.CO;2

Zhai, X., Johnson, H. L., & Marshall, D. P. (2010). Significant sink of ocean-eddy energy near western boundaries. *Nature Geoscience*, *3*(9), 608–612. https://doi.org/10.1038/ngeo943